Available online at www.sciencedirect.com
SCIENCE DIRECT®
Journal of Sound and Vibration 278 (2004) 1025–1050
JOURNAL OF SOUND AND VIBRATION
www.elsevier.com/locate/jsvi

Impact oscillations and wear of loosely supported rod subject to harmonic load ☆

J. Knudsen[a,b,*], A.R. Massih[a,c]

[a] *Division of Materials Science, Malmö University, SE 205 06 Malmö, Sweden*
[b] *Luleå University of Technology, SE 971 87 Luleå, Sweden*
[c] *Quantum Technologies AB, Uppsala Science Park, Uppsala SE 751 83, Sweden*

Received 3 June 2003; accepted 22 October 2003

Abstract

The non-linear dynamic behaviour of a damped rod oscillator with elastic two-sided amplitude constraints is analyzed using finite element method. Symmetric and asymmetric elastic double-impact motions, both harmonic and sub-harmonic, are studied by way of a Poincaré mapping that relates the states at subsequent impacts. It is found that by increasing the forcing frequency (ω) for the beam at a certain frequency a stable period one motion turns into a stable period two motion without bifurcation and subsequently moves to an infinite number of solutions characteristic of chaotic behaviour through a cyclic fold bifurcation. By further increasing ω a series of windows in the bifurcation diagram (impact velocity vs. ω) comprising periodic solutions within the chaotic domain appear. The kinds of bifurcations involved are discussed. Furthermore, impact work-rate of the beam, i.e., the rate of energy dissipation to the impacting surfaces, is calculated. Computations show that the work-rate for asymmetric orbits is substantially higher than for symmetric orbits at or near the same frequency. For the vibro-impacting beam, under conditions that exhibit a stable attractor, calculation of work-rate allows prediction of the "lifetime" of the contacting beam due to fretting-wear damage by extending the stable branch and using the local gap between contacting surfaces as a control parameter.

☆ Part of this paper was presented at the ASME International Mechanical Engineering Congress & Exposition, November 17–22, 2002, New Orleans, LA, USA.

*Corresponding author. Fax: +46-40-665-71-35.
E-mail address: tsjakn@ts.mah.se (J. Knudsen).

0022-460X/$ - see front matter © 2003 Elsevier Ltd. All rights reserved.
doi:10.1016/j.jsv.2003.10.060

1. Introduction

Oscillating mechanical systems confined within barriers exhibit highly non-linear behaviour due to impacting. These systems are prevalent in many industrial equipment such as rattling gears [1], steam generator tubes and fuel rods in nuclear power plants [2], to name just a few. The simplest model for vibro-impacting system is a spring–mass system with amplitude constraint. A single degree-of-freedom (s.d.o.f.) oscillator with one-sided elastic constraint has been studied by Shaw and Holmes [3]. They found harmonic, sub-harmonic and chaotic motions and analyzed the bifurcations leading to them. Furthermore, they concluded that zero velocity impacts (grazing) in such a system cause discontinuities in the gradient of the impact map which give rise to discontinuous bifurcation, called grazing bifurcation. Shaw [4] considered the dynamics of s.d.o.f. oscillator with two-sided rigid constraints and used a simple impact rule via a coefficient of restitution for the encounters with the constraints. He assumed that the excursions between the constraints are governed by a linear equation of motion. He analyzed the motions and their stability. By calculating frequency response curves (impact velocity vs. forcing frequency) Shaw found regions in parameter space for which there were no stable symmetric orbits having two impacts. In such regions a series of bifurcations, which resulted in long period, stable periodic and chaotic motions was found [5].

Following the findings of Shaw and Holmes [3] the details of grazing bifurcations in s.d.o.f. one-sided impact oscillators have been further explored [6–9]. It is found that a grazing bifurcation occurs when a point on the orbit of the Poincaré map intersects the line of zero impact velocity. Additional complex vibro-impact effects have been noted by Budd and Dux [10] using mathematical analysis. These comprise the phenomena of chattering and trapping (sticking). Chattering comes about when infinitely many impacts occur in a finite time and trapping when the impacting mass gets stuck to the constraint wall. These complex phenomena, grazing bifurcation, chattering and trapping, analyzed for s.d.o.f. impact oscillator, have also been evaluated for multi-d.o.f. impact oscillators, see e.g. Refs. [11–13]. In this regard, finally Qiu and Feng [14] studied the impact dynamics of thin plates by considering a single-mode impact model of a plate and then employed an equivalent s.d.o.f. impact oscillator to delineate the details of dynamic behaviour. They found periodic solutions bifurcate from the grazing bifurcation point and that most of these periodic orbits terminate at secondary grazing bifurcations.

In earlier studies the vibro-impact dynamics of beams subject to harmonic loads [15] and random loads [16] were analyzed. The results of those analyses were compared with measurements of contact forces and displacements made on a loosely supported rod in experiments. To characterize the system dynamics, a s.d.o.f. system with two-sided elastic constraints subject to both harmonic and random loads [15,16] was evaluated. A two-dimensional beam with two-diametrically opposed identical supports was modelled by finite element method. Both systems exhibited aperiodic as-well-as periodic solutions when subjected to harmonic forces. But when the systems were subjected to random forces no periodic solutions were found.

Furthermore, in a more recent study, [17,18], the details of dynamic stability of weakly damped impact oscillators with elastic constraints subject to harmonic loads were evaluated. A beam oscillator and its equivalent s.d.o.f. system was considered and stability and bifurcation analyses for the motion using the Poincaré map method to directly determine the stable periodic solution were carried out. The domains of instability of the motion were delineated and compared with

those of an equivalent s.d.o.f. oscillator system for which exact analytical solutions are available. The computations showed that the route to chaos in the s.d.o.f. harmonic system is initiated with a supercritical symmetry breaking bifurcation followed by a sequence of flip bifurcations, whereas for the beam oscillator a perturbed supercritical symmetry breaking bifurcation is followed by the Neimark bifurcations [19]. As in the present analysis, the input forcing frequency ω, in dimensionless form, was selected as control parameter to study the transitions between the different dynamic regimes.

Commonly, impacting is associated with increased wear of the components of the oscillator [20], which is related to the dynamical behaviour of the system. Hence, study of the vibro-impact dynamics is important for understanding and analyzing wear of components that are under such motions.

On a macroscopic scale removal of material from the surface due to impacts may be modelled by Archard's wear relation [21]. To relate wear volume to non-linear quantities, such as the contact forces and relative sliding motion, Frick et al. [20] introduced the concept of work-rate. Recently, the notion of the shear work-rate was proposed by Pettigrew et al. [22]. It is defined as the integral of the shear or sliding force times the sliding distance per unit time. Hence, the shear work-rate is identical to the mechanical energy dissipated at contact points. Monte Carlo simulations have been adopted to cope with the complex dynamic response as well as uncertainties in material parameters involved in vibro-impacting systems with wear. Delaune et al. [23] studied how uncertainties of parameters in wear tests influenced work-rate calculations and Charpentier and Payen [24] applied a probabilistic method to compute wear work-rate and lifetime of steam generator tubes.

In the present paper the work-rate for stable periodic solutions is evaluated. These solutions exhibit asymmetric wear of the contact sites, as the gap increases through wear. This allows the prediction of the lifetime of the studied system, i.e., the time to reach a specific wear depth at the contact sites. In earlier studies, vibro-impact dynamics were analyzed in connection with an experiment concerning wear work-rate of a beam oscillator confined within elastic barriers subject to harmonic loads [15] and stochastic loads [16]. Recently, details of dynamic stability of weakly damped beam oscillators with elastic supports have been evaluated using the Poincaré map method to determine stable periodic solutions and the work-rate associated to these solutions [17]. Here an attempt has been made to analyze the dynamic behaviour of the beam oscillator in the frequency interval $\omega \in [6, 8]$ by evaluating all the stable solutions of the Poincaré mapping. More specifically, the transition to chaotic motion for the system is evaluated.

The structure of this paper is as follows. The beam oscillator with two-sided elastic constraints is considered in Section 2. The dynamics of the system and the governing equations are presented in Section 3. Section 4 outlines the method of analysis. The wear model is described in Section 5. The results of computations are presented and discussed in Sections 6 and 7. The last section is a conclusion.

2. Oscillating beam

Consider a long slender beam supported at one end by a pair of stiff springs, namely a torsion spring suppressing rotation and a lateral (deflection) spring suppressing translation. The beam is

constrained by symmetric contact sites situated near the other end with a gap size X_0, see Fig. 1. The beam is excited with a harmonic force of frequency Ω applied in the same plane as the contact sites. The case considered was an object of an experiment, performed on a portion of nuclear fuel rod, which was analyzed in earlier papers [15,16].

For the considered beam the Bernoulli–Euler approximation that the local curvature of the beam axis is proportional to the local moment of the beam is assumed. In addition, the Rayleigh-type damping is assumed [25]. The beam is discretized in space with finite elements using cubic interpolation functions. The chosen finite element mesh consists of four elements with two degree-of-freedom at each node. Newmark's time integration method is utilized [26]. The contact sites are modelled with linear elastic springs. The developed computational program uses a node-to-node contact algorithm, hence each contact site is connected to a specific node. Each contact site can be given individual force–displacement relationship in normal, tangential, and axial directions. Stick-slip motion along the curved surface of the beam is allowed. The contact force vector $\mathbf{p}$ is resolved into $\mathbf{p} = (p_n, p_c, p_a)$, where indices n, c and a denote normal, circumferential and axial directions, respectively. Correspondingly the gap vector is decomposed as $\mathbf{g} = (g_n, g_c, 0)$. Classical contact laws (Signorini plus Coulomb) are assumed, see e.g. Refs. [15,27]. Since the present work deals with planar beams only, the circumferential components are set equal to zero. Furthermore, because the deflections are small, $p_a = 0$. Hence, friction force does not enter these calculations.

The details of the governing equation for the beam, the finite element discretization procedure and the specific conditions before and after the impact with the springs are described in Refs. [15,28]. The model has been used to analyze beam vibrations and wear work-rate in earlier papers [15,16,26,28,29] with and without friction.

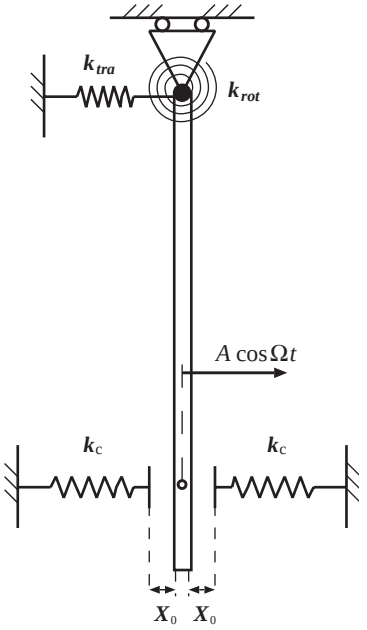

Fig. 1. The basic geometry of the cantilever impact beam oscillator with elastic supports and gap size X_0.

3. Dynamics

3.1. Equations of motion

The dynamics of the structure, described in the foregoing section, can be written in a finite element framework as a system of first order differential equations

$$\begin{aligned}\dot{\mathbf{x}} &= \mathbf{v},\\ \dot{\mathbf{v}} &= \mathbf{M}^{-1}[\mathbf{f}_a + \mathbf{f}_c - \mathbf{C}\mathbf{v} - \mathbf{K}\mathbf{x}],\\ \dot{\tau} &= 1,\end{aligned} \tag{1}$$

where $\mathbf{M}$, $\mathbf{C}$ and $\mathbf{K}$ are the consistent mass, damping and stiffness matrices, respectively; $\mathbf{x} = \mathbf{X}/X_0$ and $\mathbf{v}$ are the dimensionless displacement and velocity vectors, respectively; and $\tau = \omega_0 t$, where ω_0 is the fundamental eigenfrequency of the beam and t is the actual time. Also, $\mathbf{f}_a$ is the applied force, $\mathbf{f}_c$ is the contact force and a dot over a symbol indicates the time derivative with respect to τ. Consequently, the state vector for the system by $(\mathbf{x}, \mathbf{v}, \tau)$ is defined. The vector field defined in Eq. (1) has dimension $2n_{d.o.f.} + 1$, where $n_{d.o.f.}$ is the degrees of freedom (d.o.f.) of the system. For a harmonic load with forcing frequency Ω, the field is periodic in τ with period $2\pi/\omega$, where $\omega = \Omega/\omega_0$.

Since a node-to-node contact algorithm is used, the node x_c where structural contact will occur can be identified. Define a one-sided Poincaré section by

$$\Sigma = \{(\mathbf{x}, \mathbf{v}, \tau) | x_c = +1, v_c > 0\} \tag{2}$$

and the corresponding return map $\mathbf{P}$ by

$$\mathbf{P} = \Sigma \to \Sigma \quad \text{or} \quad (\hat{\tau}, \hat{\mathbf{x}}^r, \hat{\mathbf{v}}) = \mathbf{P}(\tau, \mathbf{x}^r, \mathbf{v}), \tag{3}$$

where $\mathbf{x}^r$ is the reduced displacement vector, meaning that the contact node $x_c = +1$ is excluded, and a caret $\hat{}$ over the state variables is used to denote the quantities at the subsequent structural contact. The algorithm for the computation of the Poincaré map $\mathbf{P}$ has been detailed in Ref. [17].

3.2. Periodic orbits

The stability of periodic orbits is analyzed by means of the Poincaré return map. For a beam oscillator a fixed point of the return map $\mathbf{P}$ in Eq. (3), i.e., harmonic motion of the equation system (1), satisfies the following condition

$$\left(\bar{\tau} + \frac{2\pi n}{\omega}, \bar{\mathbf{u}}\right) = \mathbf{P}^k(\bar{\tau}, \bar{\mathbf{u}}), \tag{4}$$

where $\mathbf{P}^k$ indicates that $\mathbf{P}$ has been applied k times, n denotes the sub-harmonic of the k iterated map and the point $(\bar{\tau}, \bar{\mathbf{u}})$ is referred to as periodic point of $\mathbf{P}$, with $\mathbf{u} = (\mathbf{x}, \mathbf{v})$ denoting a vector comprising displacements and velocities and the bar over a variable indicates the periodic point. The local stability of the periodic point is analyzed by the eigenvalues of the Jacobian matrix $\mathbf{P}^k$ evaluated at the periodic point. More details on the computational method can be found in Ref. [17].

4. Analysis method

The procedure of computing one or more iterates of the Poincaré return map, given by Eq. (3), is to start from the initial state $(\tau, \mathbf{u})$ with $x_c = +1$, then step forward in time until $\hat{x}_c(\hat{\tau}) = +1$ for $\hat{\tau} > \bar{\tau}$, where $\hat{\tau}$ denotes the time at the subsequent impact at the same contact site. An effective time-stepping algorithm has been employed to accurately determine the time between impacts [17].

4.1. Fixed points

Fixed points (periodic orbits) of the Poincaré map defined by Eq. (3) are sought using a globally convergent Newton iteration method for finding the roots of the system of equations

$$\mathbf{P}^k(\bar{\tau}, \bar{\mathbf{u}}) - \left(\bar{\tau} + \frac{2\pi n}{\omega}, \bar{\mathbf{u}}\right) = 0. \tag{5}$$

Here the term global refers to a method which converges to a solution for almost any starting point. The particular algorithm used here has been adapted from [30].

4.2. Branches and manifolds

Sequential continuation is used to map out branches of fixed point solutions, e.g. Ref. [31]. Let α denote the control parameter for the problem. The interval of interest is divided into closely spaced grid points $\alpha_0, \alpha_1, \ldots, \alpha_N$. The solution $(\bar{\tau}_j, \bar{\mathbf{u}}_j)$ at α_j is used as a prediction for the next solution $(\bar{\tau}_{j+1}, \bar{\mathbf{u}}_{j+1})$ at α_{j+1}. The predicted value is then corrected with the Newton iteration scheme presented in the preceding section.

The sequential continuation scheme will obviously fail at bifurcation points where two or more branches meet, e.g., symmetry breaking bifurcations. In practice, however, sufficiently small increments in the control parameter can be chosen to prevent the fixed point from jumping from one branch to another [32].

Another key issue in non-linear dynamics is the existence of stable and unstable manifolds of fixed points, denoted by $\mathcal{W}^s$ and $\mathcal{W}^u$, respectively. These manifolds are split into two half-manifolds by excluding the fixed point. These are denoted by $\mathcal{W}^s_{1/2}$ and $\mathcal{W}^u_{1/2}$ for stable and unstable half-manifolds, respectively. Stable and unstable half-manifolds of a fixed point are found using the well established algorithm proposed by Parker and Chua [33].

5. Wear model

5.1. The model

Fretting wear of impacting structures can be modelled by using Archard's wear law [21], which states that loss of material is related to contact force times the sliding distance through some material parameters. In a one-dimensional system this makes no sense, since no sliding can take place. In this paper it is assumed that the material loss or damage can be related to the impact

energy and that all damage occurs at the contact sites, according to

$$\Delta V = k\langle W\rangle \Delta T, \tag{6}$$

where ΔV is the volume loss due to wear, k is a material-dependent parameter, $\langle W\rangle$ is the time averaged impact work-rate and ΔT is the wear process time.

The impact work-rate parameter, is thus essentially a measure of available power to produce damage at the supports. Following Ref. [15] the incremental impact work-rate is defined as $\mathrm{d}U = p\,\mathrm{d}s$, where p and s denote contact force acting on the support and its displacement, respectively. Returning to the global variables, defined in the foregoing section, the work-rate increment connected to contact site i is written as

$$\begin{aligned} \mathrm{d}W_i &= k_c(|X - X_i|)\,\mathrm{d}(|X - X_i|) \\ &= k_c(|X - X_i|)\,|\dot{X}|\,\mathrm{d}t, \end{aligned} \tag{7}$$

where $\dot{X} = \mathrm{d}X/\mathrm{d}t$.

Work-rate at individual contact sites is written as

$$\mathrm{d}w_i = [|x - x_i|]\,|v|\,\mathrm{d}\tau, \tag{8}$$

where $\mathrm{d}w = \mathrm{d}W/(k_c X_0^2)$ and $v = \partial x/\partial\tau$. Note that, impacts occurring at $x = +x_1$ and $-x_2$ are accounted for by taking the absolute value of x. The time averaged work-rate is consequently

$$\langle w\rangle_i = \frac{1}{\tau_m - \tau_0}\int_{\tau_0}^{\tau_m} [|x| - x_i]\,|v|\,\mathrm{d}\tau, \tag{9}$$

where τ_0 is the time from which the iteration is initiated and τ_m is the time after m iterations of the map $\mathbf{P}$. The change of sign in v is accounted for in the integrand.

5.2. Evaluation of gap

In an earlier work it was found that the impacting beam oscillator, presented in Section 2, has stable periodic solutions, for which the symmetrically placed contact sites experience asymmetric work-rate [17].

The contact sites are regarded as one-dimensional and it is assumed that damage only occurs at contact sites, hence the volume loss is proportional to the gap increment. Using Eq. (6), the gap increment for the individual contact sites is written as

$$\Delta X_i \sim \langle W\rangle_i \Delta T \quad \text{for } i = 1, 2, \ldots, N, \tag{10}$$

where ΔX_i denotes the gap increment at contact site i and N is the number of contact sites.

Using the gap connected to contact site 1 as a control parameter in the computations, the gap evolution at all other contact sites is found through

$$\Delta X_i = \frac{\langle W\rangle_i}{\langle W\rangle_1}\Delta X_1. \tag{11}$$

The time to reach this wear depth (gap) is found from Eq. (10) in the form, viz.

$$\Delta T = \frac{\Delta X_i}{k' \langle W \rangle_i}, \tag{12}$$

where $k' = k/S$ and S is the cross sectional area of the contact site.

Eqs. (11) and (12) expressed in non-dimensional form become

$$\Delta x_i = \frac{\langle w \rangle_i}{\langle w \rangle_1} \Delta x_1 \quad \text{and} \quad \Delta \mathscr{T} = \frac{\Delta x_i}{\langle w \rangle_i}. \tag{13}$$

Note that the non-dimensional wear process time $\Delta \mathscr{T}$ comprises the material parameter k'.

6. Results of computations

6.1. Routes to chaos

The Poincaré map method, described in Section 3, has been employed to directly determine the stable periodic solutions. From these solutions the solution branches can then be followed by sequential continuation, according to the methods described in the foregoing sections. The response of the system to the input frequency is evaluated, i.e., the impact velocity v vs. forcing frequency ω, where ω is taken as the control parameter for the system.

In an earlier analysis a bifurcation diagram was presented, $\bar{v}$ vs. ω, for stable and unstable period-one solutions in the first sub-harmonic of the system for $\omega \in [3, 11]$ by using relation (4) [17]. In that analysis, no stable or unstable branches of period-one solutions were found in the interval $\omega \in [6.508, 7.343]$, see Ref. [17, Fig. 13].

In the present work an attempt has been made to analyze the dynamics of the system in the frequency interval $\omega \in [6, 8]$ by evaluating all the stable solutions of relation (3). The results of the computations are presented in form of bifurcation diagrams, where the response of system (impact velocity) to the input frequency is evaluated. In addition, phase portraits and time histories at certain frequencies are displayed to illustrate the dynamic behaviour of the system. The dynamics of the beam oscillator have been explored by studying its motion at the contact node. The structural properties of the beam oscillator, Fig. 1, are listed in Table 1 [15].

Table 1
Properties of impact beam oscillator

Beam density	ρ	kg/m^3	9347.51
Cross section area	$\mathscr{A}$	m^2	7.088×10^{-5}
Beam length	L	m	0.64
Mass proportional damping	c_m	s^{-1}	0.3984
Stiffness proportional damping	c_k	s	2.975×10^{-5}
Flexural rigidity	D	N m^2	24.90
Support lateral spring stiffness	k_{tra}	N/m	1.48×10^5
Support torsion spring stiffness	k_{rot}	N m/rad	5.35×10^2
Contact spring stiffness	k_c	N/m	123,750
Force amplitude	A	N	6
Gap	X_0	m	1.25×10^{-4}

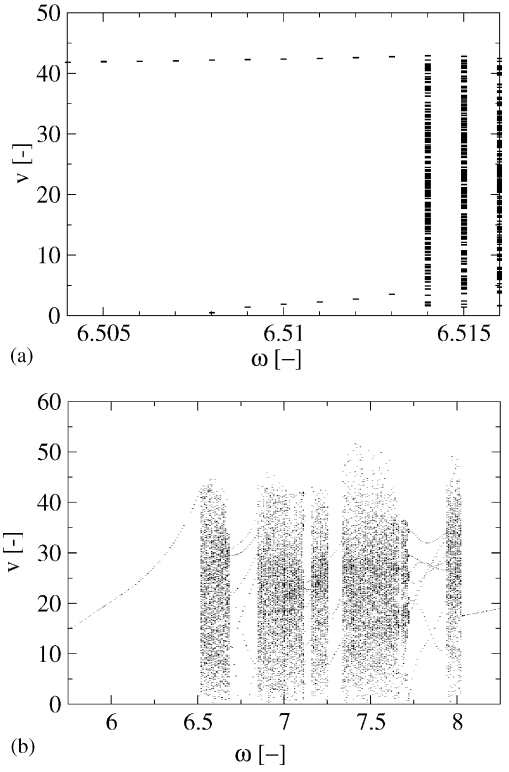

Fig. 2. Impact velocity v vs. forcing frequency ω for the beam oscillator, (a) $\omega \in [6.504, 6.516]$, (b) $\omega \in [5.75, 8.25]$. Note that for each ω, 200 consecutive impact velocities are plotted and that each impact velocity is marked with a "-" symbol.

Figs. 2a and b show the impact velocity v vs. the forcing frequency ω in the intervals $[6.504, 6.516]$ and $[5.75, 8.25]$, respectively. The data are taken from the Poincaré section at the position of the structural contact. Two hundred consecutive impact velocities are recorded and plotted in the figures for each forcing frequency. These 200 impact velocities are the last of 1000 iterates of the return map, Eq. (3). These results indicate that at $\omega = 6.505$ there is a stable period-one motion (solution), which turns into a period-two motion at $\omega \approx 6.508$ without bifurcation. The motion then becomes chaotic at $\omega \approx 6.514$, i.e., as ω increases the periodic solutions explode to a plethora of solutions.

The diagrams in Figs. 3 and 4 show the phase portraits at the contact node for $\omega = (6.505, 6.510, 6.51305)$. The associating time histories, displacement vs. time, for $\omega = (6.505, 6.515)$ are shown in Fig. 5. The corresponding power spectral density (PSD), i.e., the displacement PSD vs. the response frequency of the structure (Fourier transform of the time history) is presented in Fig. 6.

6.1.1. *Remarks on dynamics*

As mentioned in the foregoing section when ω is raised from $\omega \approx 6.505$ to 6.510, the stable period-one motion passes into a stable period-two motion without bifurcation, i.e., the Floquet multipliers λ_i (of the Poincaré map) remain within the unit circle [19]. From Fig. 2a it can be see

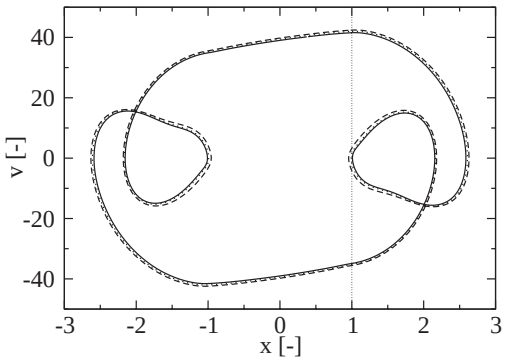

Fig. 3. Phase portraits, velocity v vs. displacement x, of the first sub-harmonic of the beam oscillator at the point where impact can occur at the stable period-one solutions, $\omega = 6.505$ (solid line), stable period-two solutions $\omega = 6.510$ (dotted line) and at $\omega = 6.51305$ (broken line).

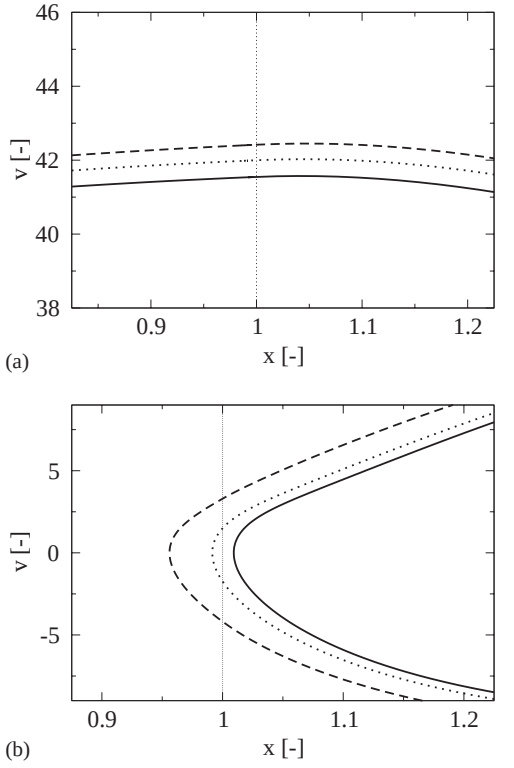

Fig. 4. Zoomed sections of the phase portraits displayed in Fig. 3: (a) at the impact region, (b) in the "loop" region. $\omega = 6.505$ (solid line), $\omega = 6.510$ (dotted line), $\omega = 6.51305$ (broken line).

that at $\omega = 6.505$ the orbit intersects the Poincaré section at one point, $v \approx 42$, whereas at $\omega = 6.510$ the orbit intersects the Poincaré section two times at $v \approx 2$ and 42. The phase portraits for the two motions are very close (Fig. 3). However, a closer look at a portion of the phase portrait in

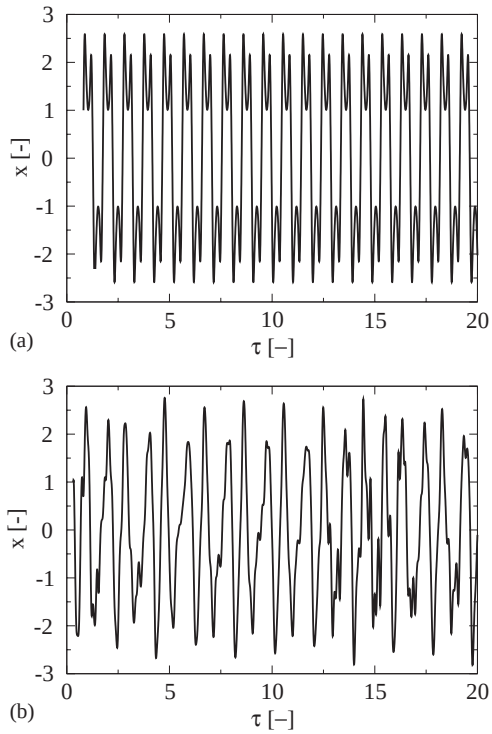

Fig. 5. Displacement x vs. time τ for the beam oscillator: (a) at $\omega = 6.505$, (b) at $\omega = 6.515$.

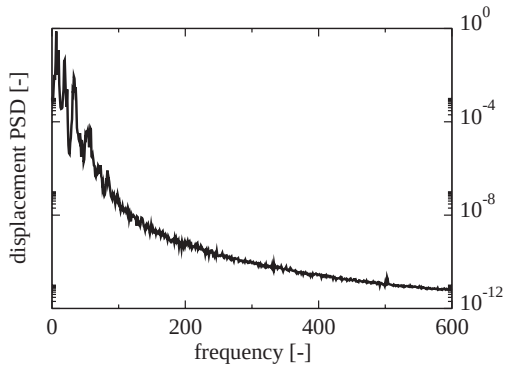

Fig. 6. The displacement power spectral density vs. frequency response at $\omega = 6.515$.

the proximity of $x \approx 1$ (Fig. 4) reveals the difference between the orbits. Fig. 7a displays the response of the system, contact velocity, for ω varying in the range $[6.500, 6.5131]$. It shows the transition from the stable period-one motion to a stable period-two motion at $\omega = 6.508$ and finally at $\omega = 6.5131$ to an unstable state. This latter kind of behaviour, where a branch of stable periodic solutions and a branch of unstable solutions, which exist for $\lambda \leqslant \lambda_c$, collide and annihilate each other at the bifurcation point $\lambda_c = 1$ is a characteristic of *cyclic-fold bifurcation point* [19].

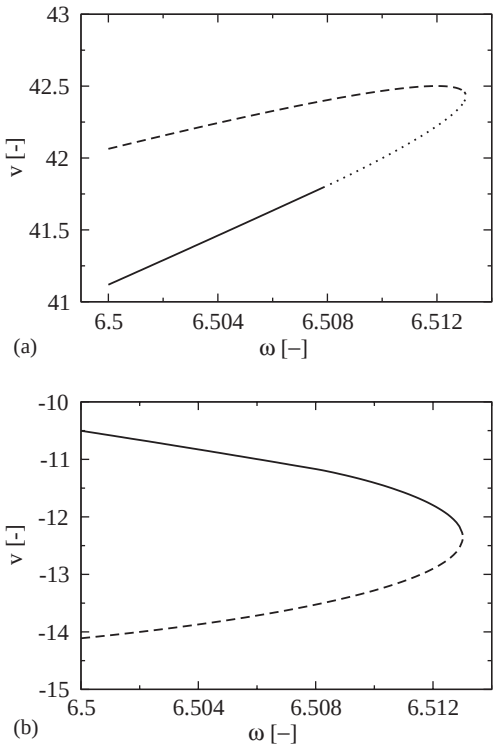

Fig. 7. Bifurcation diagrams, (a) Impact velocity v vs. forcing frequency ω in a spatial Poincaré plane: One-period (solid line) → two-period (dotted line) → cyclic fold → unstable (broken line). (b) Velocity vs. forcing frequency in a time domain Poincaré plane: One-period stable (solid line) → cyclic fold → unstable one-period (broken line).

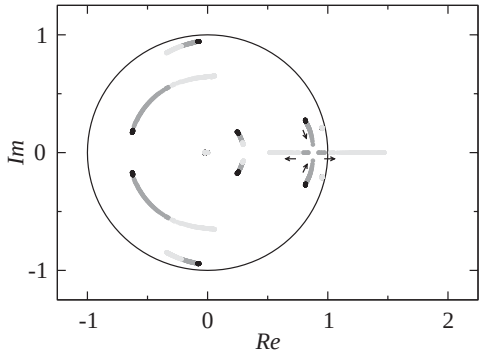

Fig. 8. Eigenvalues of the Jacobian matrix $\mathbf{P}^k$ close to the cyclic-fold bifurcation at $\omega = 6.5131$. Black, dark grey and light grey circles, mark eigenvalues connected to stable period-one, stable period-two and unstable solutions, respectively.

This is illustrated in Fig. 8, showing the eigenvalues of the Jacobian matrix of $\mathbf{P}^k$ to the return map (4). It shows one eigenvalue escaping the unit circle through $+1$, while the rest remain confined within the circle, as the system passes through the bifurcation point. It should be noted

that this transition occurs without period-doubling bifurcations as the excitation frequency is increased.

The transition from a period-one orbit of the first iterated map to a period-one orbit of the second iterated map occurs without bifurcation, for which the index k in Eq. (4) switches from 1 to 2. This can be illustrated by studying the details of the dynamics using a Poincaré section in the time domain

$$\Sigma_t = \left\{ (\mathbf{x}, \mathbf{v}, \tau) \middle| \tau = 0, \mathrm{mod}\, \frac{2\pi}{\omega} \right\}. \tag{14}$$

Fig. 7b shows the stable and unstable branches of period-one orbits leading to the cyclic fold bifurcation using the time domain Poincaré section. As can be seen the discontinuity at $\omega \approx 6.508$ is no longer visible. The discontinuity arises as the impact velocity passes through zero, see Fig. 4. This in turn causes the eigenvalues of the Jacobian matrix of the return map (4), to tend to infinity, which is a characteristic of a grazing bifurcation, causing the numerical method to fail. However, using the time domain Poincaré section the eigenvalues remain within the unit circle. Hence, the transition from a one- to a two-impact one-period orbit, is not a grazing bifurcation, since a grazing bifurcation generates discontinuities in gradient of any Poincaré map [9].

It can be seen from Fig. 5b that the time history of the motion is non-periodic at the frequency $\omega = 6.515$. In Fig. 6b the power spectrum density for the motion at $\omega = 6.515$ is shown. The diagram displays the frequency content of the Fourier transform of the displacement. As can be noted no distinct spikes are observed from this plot, hence implying that chaotic motion is prevalent at $\omega = 6.515$. Moreover, from Fig. 2b four vertical windows in $\omega \in [6.5, 8]$ in which multiple periodic solutions emerge can be seen. In the fourth window, $\omega \in [7.65, 7.95]$, the orbit intersects the chosen Poincaré section eight times for a period $7 \times 2\pi/\omega$ motion. Hence, the branches can be seen as fixed points to the eighth iterated map. To study the transition to aperiodic motion, as ω decreases, it is advantageous to switch to a time domain Poincaré section defined by Eq. (14). The route is initiated with a Neimark bifurcation at $\omega \approx 7.72125$, i.e., two complex conjugate eigenvalues leave the unit circle simultaneously, away from the real axis, see Fig. 9. The resulting dynamics, in the fourth window, is exemplified in forms of phase portraits in Fig. 10.

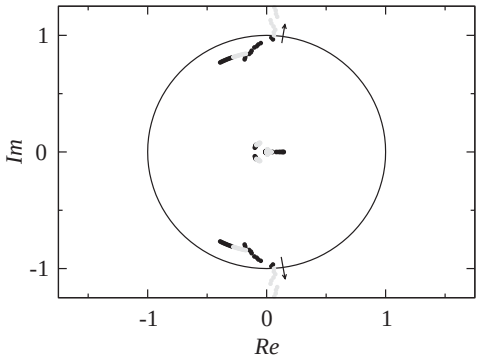

Fig. 9. Eigenvalues of the Jacobian matrix $\mathbf{P}^k$ close to a Neimark bifurcation at $\omega \approx 7.7213$. Black and light grey circles mark eigenvalues connected to stable and unstable period-seven solutions, respectively.

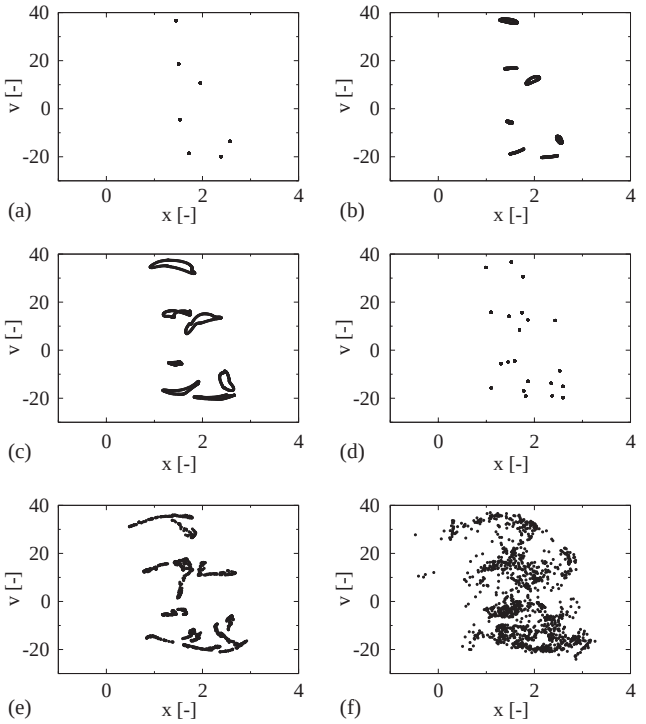

Fig. 10. Phase portraits, velocity v vs. displacement x, of the stable period-seven orbit undergoing a Neimark bifurcation; (a) $\omega = 7.75$, (b) $\omega = 7.715$, (c) $\omega = 7.68$, (d) $\omega = 7.67$, (e) $\omega = 7.655$ and (f) $\omega = 7.64$. The Neimark bifurcation occurs between (a) and (b). The figures display velocity and displacement at 1400 intersections with the chosen time domain Poincaré section. Each intersection is marked with a black circle.

In the first window in Fig. 2b, $\omega \in [6.68, 6.84]$, the transition to aperiodic motion coincides with a Neimark bifurcation, as the forcing frequency is decreased through $\omega = 6.68$. Note also that in the third window in Fig. 2b, $\omega \in [7.258, 7.342]$, there is an asymmetric period-three orbit, see Fig. 11a. Hence, there exists a stable four-impact period-three mirror orbit in the same region. This is shown in Fig. 11b.

6.2. *Wear analysis*

In this section the results of impact wear computations, for the considered impact beam oscillator (Fig. 1), are presented. The Poincaré map method described earlier, is utilized to find fixed periodic points of the system. The gap x_1, at the right hand contact site in Fig. 1 (initially at $x = +1$), is used as a control parameter. The sequential continuation method [17] is employed to compute the evolution of the wear depth. All computations have been made with the structural properties and conditions listed in Table 1. These properties concern a portion of a nuclear fuel rod vibrating in air [15].

6.2.1. *Impact work rate*

In an earlier analysis [17] the dynamic response of the considered impact beam oscillator, in the frequency interval $\omega \in [3, 11]$, was studied and branches of stable period-one solutions were

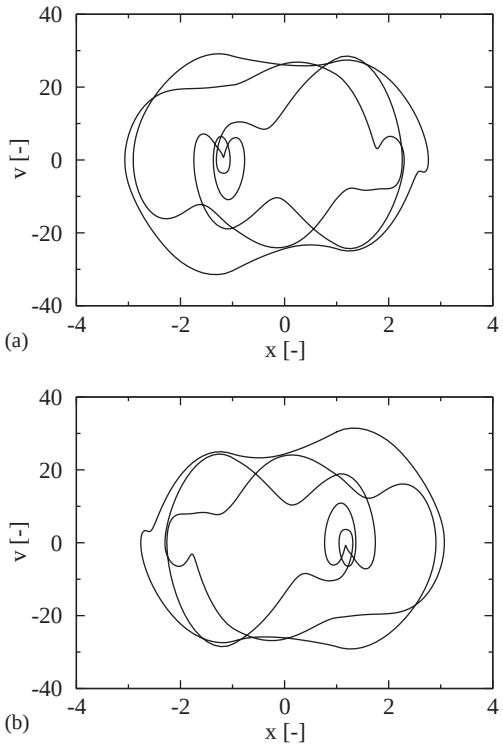

Fig. 11. Orbit in the phase plane in the third window in Fig. 2, velocity v vs. displacement x, at $\omega = 7.3$ (a) stable three-impact period-three orbit and (b) stable four-impact period-three mirror orbit.

identified. Furthermore, the impact work-rate was evaluated along these branches. It was found that a stable periodic solution could lead to asymmetric wear of the symmetrically placed contact sites. In the present work an attempt has been made to analyze the time evolution of such points through wear of the contact sites.

Figs. 12a and b show the impact work-rate along two different branches of stable period-one solutions, exhibiting different work-rates at the initially symmetrically placed contact sites. These figures show the work-rate evaluated at right hand contact site 1 (at $x = +x_1$) and at the left hand contact site 2 (at $x = -x_2$).

From the stable branches shown in Fig. 12 two frequencies were selected for further evaluation, namely $\omega = 5.610$ and 9.900. At these frequencies the evolution of gap and work-rate are computed as the gap increase due to wear, according to the wear law given in Section 5. Figs. 13a and b show the gap ratio, i.e., gap at site 2 (x_2) normalised with the gap at site 1 (x_1) plotted against the gap at site 1; whereas Figs. 14a and b show the work-rate for each contact vs. the gap at site 1.

In Fig. 13a it can be seen that initially x_1 increases faster than x_2 due to the difference in work-rates (Fig. 14a). However, this difference quickly diminishes as x_1 increases, then at $x_1 \approx 1.2$ the trend suddenly reverses. This is visible in Fig. 13a as the gap ratio starts to increase. At $x_1 \approx 1.34$ an abrupt change in the work-rate is visible (Fig. 14a) and the gap ratio increases at a slower rate,

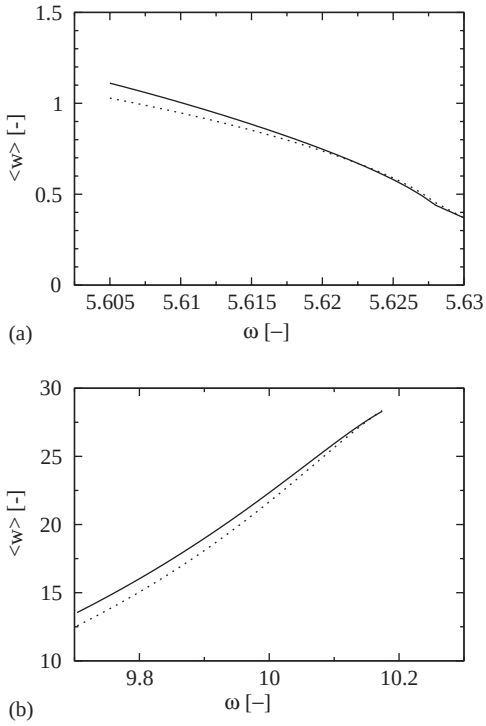

Fig. 12. Impact work-rate $\langle w \rangle$ at contact sites 1 (solid line) and 2 (dotted line) along stable branches of period-one solutions in the frequency interval (a) $5.604 < \omega < 5.631$, (b) $9.704 < \omega < 10.174$.

see Fig. 13a. Note that, as the wear process continues the system tends towards a symmetric gap. At the higher frequency the situation is different. The initially symmetric gap becomes gradually more asymmetric (Fig. 13b), which is connected to an increasing difference in work-rate between the two contact sites (Fig. 14b).

6.2.2. *Wear lifetime*

The lifetime or the time to reach a certain wear depth at the contact sites is estimated by utilizing Eq. (13). Figs. 15a and b show the gap size connected to the contact sites for $\omega = 5.610$ and 9.900, respectively.

For $\omega = 5.610$, the growth of the two gaps (x_1 and x_2) are virtually identical (cf. Fig. 15a). The evolution of the gap follows the evolution of the work-rate (Fig. 14a). For $1 \leqslant x_i \leqslant 1.34$, $i = 1, 2$ the work-rate decreases as the gap increases, see Fig. 14a. This behaviour is also reflected in Fig. 15a, where the gap growth rate (slope of curves) decreases in this interval. For gaps $x_i > 1.34$, $i = 1, 2$, the work-rate increases with gap size, which in turn leads to a gradual increase of gap growth rate, see Fig. 15a.

For $\omega = 9.900$ the gap growth rate increases as the wear process continues, see Fig. 15b. It can also be seen that the system becomes increasingly asymmetric with time, since the gap at contact site 1 grows faster than at site 2, i.e., $\langle w \rangle_1 > \langle w \rangle_2$.

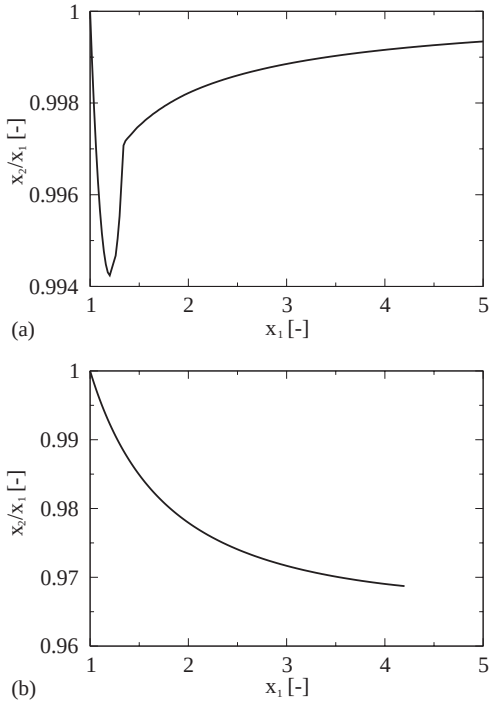

Fig. 13. Gap ratio x_2/x_1 between contact sites 1 and 2 vs. gap size x_1 at forcing frequencies (a) $\omega = 5.610$, (b) $\omega = 9.900$.

6.2.3. Remarks on wear

In the foregoing section a sharp change in work-rate, as the gap increases through $x_1 = 1.34$ for the case $\omega = 5.610$ (Fig. 14a), was calculated. This change is connected to a qualitative change in the dynamics of the system. In Ref. [17] it was noted that a more "wrinkled" phase orbit displayed higher work-rate compared to a smooth orbit. The shape of the phase orbits for different gap sizes, $x_1 = 1.28$ (solid line) and $x_1 = 1.40$ (broken line) for $\omega = 5.610$ are shown in Fig. 16. As the gap increases there are two competing effects, (i) the work-rate decreases where the phase orbit becomes smoother and (ii) the work-rate increases as the velocity of the impacting body increases with the growing gap.

For $\omega = 9.900$ the gap evolution through wear could be followed up to a gap size of $x_1 \leqslant 4.20$, cf. Figs. 12b, 13b and 14b. For $x > 4.20$, impacts no longer occur at the contact sites for the steady state motion of the oscillator. Hence, no further wear of the contact sites can take place.

Lifetime predictions are usually made with the work-rate computed for the initial gap, $\langle w \rangle_i^0$, through $\Delta\tau = \Delta x_i / \langle w \rangle_i^0$ [24], i.e., a linear relationship between wear depth and wear process time is assumed. This linear approach can lead to either an over- or an under-estimation of the lifetime by a factor of more than two, depending on the forcing frequency, compared to the incremental approach used to generate the curves presented in Figs. 15a and b. Note that the work-rate computed for the initial gap can be read from Figs. 14a and b. For example, for the two cases studied here, to reach a wear depth twice the size of the initial gap, the linear approach leads to

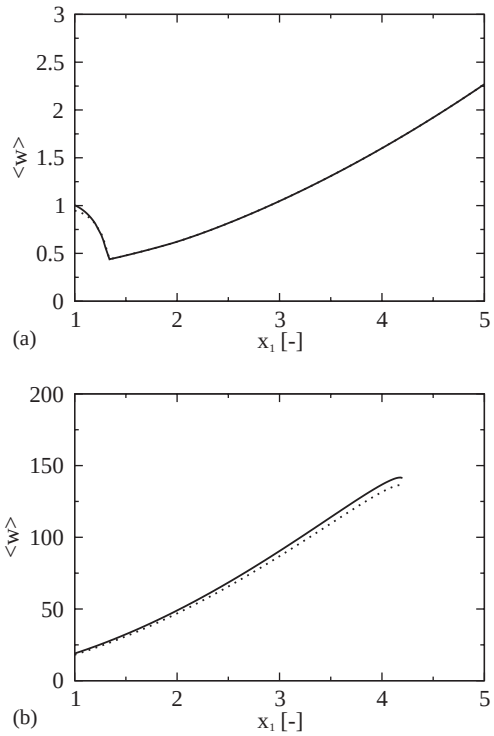

Fig. 14. Impact work-rate $\langle w \rangle$ at individual contact sites 1 (solid line) and 2 (dotted line) vs. gap size x_1 at forcing frequencies (a) $\omega = 5.610$, (b) $\omega = 9.900$.

lifetime under-estimation by a factor 1.48 for $\omega = 5.610$ and an over-estimation by a factor of 2.2 for the case with $\omega = 9.900$, see Figs. 15a and b.

The difference in estimated lifetime between $\omega = 5.610$ and 9.900 is also noteworthy (cf. Figs. 15a and b). This difference is connected to the calculated differences in work-rate, see Figs. 14a and b.

Global stability is an important topic concerning the validity of predicting wear lifetime by following stable branches. Global stability here means that the system is attracted to a certain fixed point for almost any given initial condition or at least for a controlled sub-set of initial conditions, i.e., a basin of attraction can be determined for the fixed point. Hence, if the disturbances are small enough for the system to remain within the basin of attraction, the system will return to the known fixed point after a finite time and work-rate evaluated at this point can be used to follow the evolution of the wear for the system.

If the system exhibits both saddle nodes and stable foci, knowledge can be acquired about the basin boundary by studying the stable and unstable manifolds of the saddle nodes using the algorithm proposed by Parker and Chua [33]. Note that the algorithm is only applicable to one-dimensional manifolds. Hence, the Jacobian matrix evaluated at the saddle node can only have one eigenvalue with magnitude greater than one. For other situations it is necessary to revert to brute force number crunching techniques.

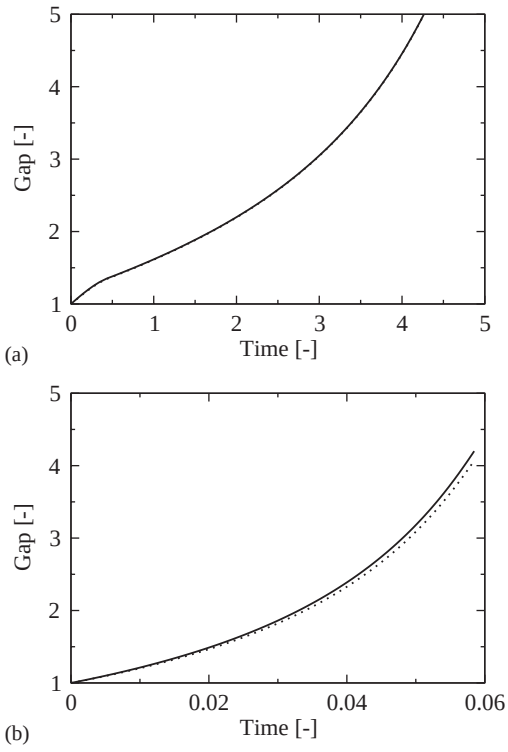

Fig. 15. Gap size x_i at individual contact sites 1 (solid line) and 2 (dotted line) vs. wear process time at forcing frequencies (a) $\omega = 5.610$, (b) $\omega = 9.900$.

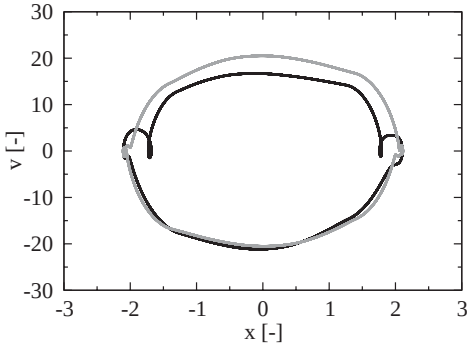

Fig. 16. Phase portraits, velocity v vs. displacement x, at $\omega = 5.610$ with gaps $x_1 = 1.28$ (black line) and $x_1 = 1.40$ (grey line), respectively.

At $\omega = 5.610$ there are two branches of stable asymmetric orbits. One stable branch is destroyed in a cyclic fold bifurcation, as it collides with a branch of unstable symmetric solutions, the other branch switches to a stable symmetric solution as ω is increased beyond the cyclic fold bifurcation point, see Fig. 17. In Ref. [17] this bifurcation was erroneously branded as a supercritical symmetry breaking bifurcation. The added numerical resolution close to the

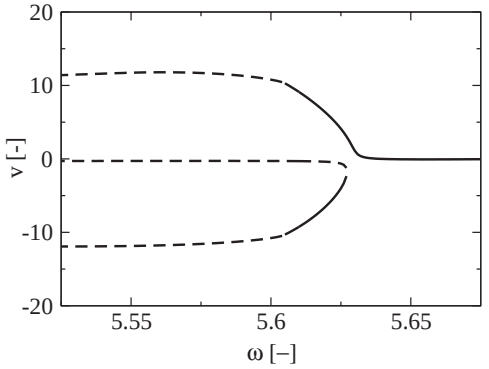

Fig. 17. Bifurcation diagram showing velocity at the contact node v vs. forcing frequency ω. Stable and unstable solutions are denoted by solid and broken lines, respectively.

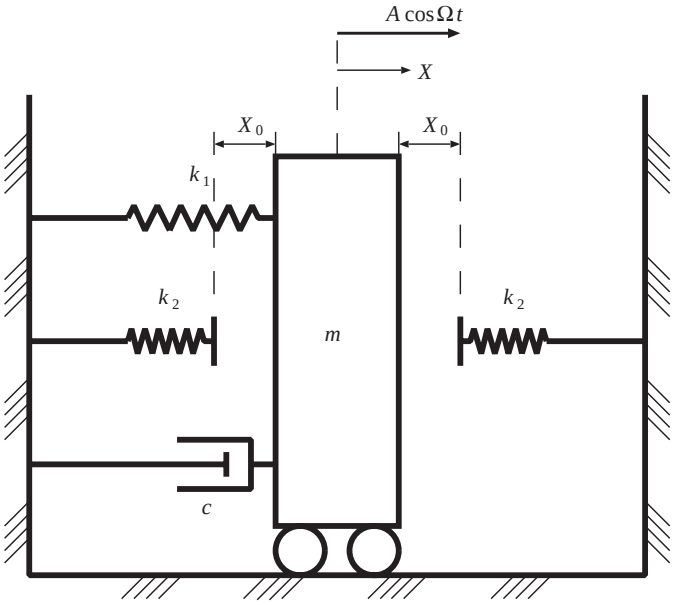

Fig. 18. A two-sided s.d.o.f. damped harmonic oscillator with elastic supports.

bifurcation point was achieved here by studying the dynamics using a time domain Poincaré section as defined in Eq. (14). This behaviour is indicative of a perturbed symmetry breaking bifurcation. Similar behaviour can also be found in an one-dimensional representation of the oscillating beam, i.e., a single degree-of-freedom oscillator with equivalent structural properties. However, in the s.d.o.f. system the symmetry bifurcation is intact. The intention is to use the s.d.o.f. system to gain insight for the complex beam system.

For the s.d.o.f. oscillator considered in Ref. [17], see the appendix and Fig. 18, the symmetry breaking bifurcation occurs at $\omega \approx 4.6215$. At $\omega = 4.4$, prior to the symmetry breaking

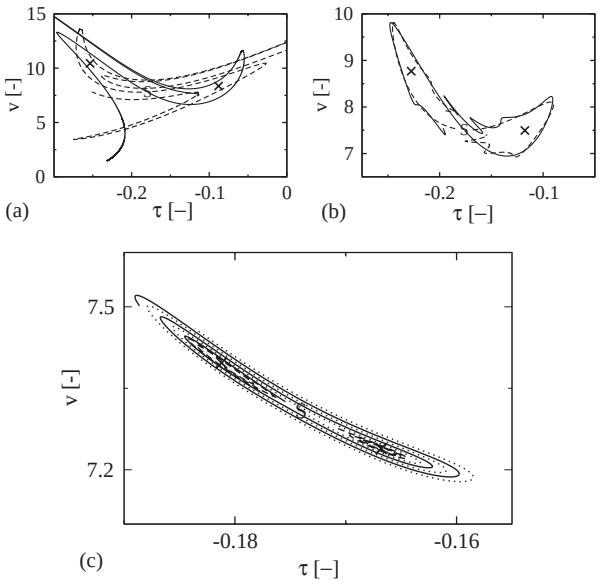

Fig. 19. The stable (solid lines) and unstable (broken lines) half-manifolds for the s.d.o.f. impact oscillator at $\omega = 4.4$, and (a) $\beta = 51.0997$, (b) $\beta = 45.0$ and (c) $\beta = 41.1$. β denotes the amplitude of the excitation force. Symbols $\times$ and S show the location of stable foci and saddle nodes, respectively. Note that, a dotted line is used for one of the stable half-manifolds in (c) to clarify the plot.

bifurcation, there exist two stable points and one unstable point. By mapping the stable and unstable half-manifolds, $\mathcal{W}^s_{1/2}$ and $\mathcal{W}^u_{1/2}$, to the unstable node, insight can be gained on how the basins of attraction for the stable points evolve as gap increases. Due to the scaling of variables, increasing the gap through wear is equivalent to decreasing the amplitude of the excitation force. Plots in Fig. 19 show computed half-manifolds for the s.d.o.f. oscillator for three different excitation amplitudes, $\beta = 51.0997$ in Fig. 19a, $\beta = 45.0$ in Fig. 19b and $\beta = 41.1$ in Fig. 19c. From Fig. 19a it is seen that the $\mathcal{W}^s_{1/2}$ and $\mathcal{W}^u_{1/2}$ intersect. Once they intersect they must intersect infinitely many times, since the manifolds are invariant sets to the saddle point [34]. Moreover, $\mathcal{W}^s_{1/2}$ and $\mathcal{W}^u_{1/2}$ here are for the same fixed point, hence they are homoclinic intersections. This also occurs at $\beta = 45.0$, Fig. 19b, however, at this wear depth (excitation amplitude) the strong stretching and folding action which occurs close to the saddle point is more visible. This stretching and folding is a feature of the Smale horseshoe map, which in turn implies sensitivity to initial conditions, a hallmark of chaos [35]. In Fig. 19c, it can be seen how $\mathcal{W}^u_{1/2}$ spiral towards the stable foci. The stable manifolds, $\mathcal{W}^s_{1/2}$, divide the studied phase space into two regions. In one region the motion is attracted to the left-hand stable focus and vice versa. Hence, the case of $\beta = 41.1$ can be considered as globally stable, since either of the stable foci will attract the motion. The equations used to generate Fig. 19 are provided in the appendix.

Returning now to the beam oscillator, Fig. 20 displays $\mathcal{W}^u_{1/2}$ extending from the saddle point. From this figure it is seen that $\mathcal{W}^u_{1/2}$ spiral towards the left-hand and right-hand stable foci as in the case of $\beta = 41.1$ in the s.d.o.f. system, Fig. 19c. This suggests that the system is globally stable for $\omega = 5.61$ and that it is possible to predict the wear lifetime as described in Section 6.2.2.

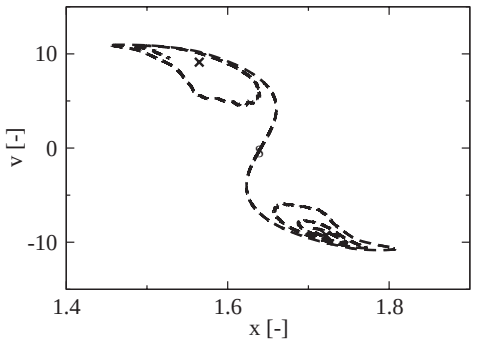

Fig. 20. The unstable half-manifolds (broken lines) (for the impact beam oscillator at $\omega = 5.610$ with gaps $x_1 = x_2 = x_0$. Symbols $\times$ and S show the location of stable foci and saddle node, respectively.

7. Discussion

The route to chaotic motion can be via period-doubling bifurcations, quasi-periodic motion and intermittency, e.g. Ref. [19]. Another road to chaos involves sudden changes in the behaviour of strange attractors with variation of a control parameter. Such changes are caused by the collision of the strange attractor with an unstable periodic orbit or, equivalently, with its stable manifold. The phenomena have been called crises [36].

Detailed evaluations of the attractors in the ω region of interest are required to study the route to chaos for the beam oscillator considered here. Likewise, as mentioned in Section 1, mathematical and numerical analyses made on s.d.o.f. and multi-d.o.f. impacting harmonic oscillators have revealed a variety of complex behaviour, such as grazing bifurcations, chattering and trapping. The method outlined in this note can be extended and used to study some of these details for continuous vibrating systems, having infinite degree-of-freedom, such as beams, tubes, etc.

To correctly identify bifurcations it is necessary to study the dynamics using more than one Poincaré section. In this analysis, two different sections were used, one was placed at the point of structural contact and another was put in the time domain. The spatial Poincaré section enables comparison with an equivalent s.d.o.f. system for which the analytical solution is known (see the appendix). Furthermore, if a fixed point solution, corresponding to an asymmetric phase orbit, is found, the mirror solution is immediately identifiable, cf. Fig. 11. However, the spatial Poincaré section leads to numerical difficulties when the system changes the number of impacts per period without bifurcating (Section 6.1.1). This problem is circumvented by using the temporal Poincaré section.

The evolution of wear for the initially symmetric system is analyzed by following the branches of stable solutions, using an Archard's type wear law to predict wear damage. Starting from an asymmetric stable orbit, it is shown that the differences in work-rate lead to a system which initially becomes more asymmetric as material is worn off at the contact sites. This behaviour can reverse, due to changes in the dynamic response. Hence, the system tends toward geometric symmetry again, see Fig. 13a. Note that the opposite also occurs, i.e., the system becomes

gradually more asymmetric, cf. Fig. 13b. Once the evolution of gap at contact sites (wear depths) and corresponding work-rates are known the lifetime of system can be computed. Here lifetime is defined as the time to reach a specified wear depth or gap size. For the cases studied here, the relationship between work-rate and gap-size is non-linear (Fig. 14). This leads to a non-linear relationship between gap-size and lifetime (Fig. 15). Hence, it is not feasible to predict lifetime or to compute the wear coefficient in Eq. (6) using a single work-rate value.

8. Conclusion

The asymmetric elastic double-impact motions of a harmonically excited cantilever type beam with two-sided elastic amplitude constraints are discussed. It is shown that the considered beam oscillator undergoes a cyclic fold bifurcation at $\omega \approx 6.5135$ leading to chaotic motion as ω is increased beyond the bifurcation point. The chaotic regime persists until $\omega > 8$. Windows of stable multi-periodic solutions are found within the chaotic regime. In the interval $\omega \in [7.65, 7.95]$, the route to chaos is initiated with a Neimark bifurcation as ω is decreased. The complete route is visualized by plotting the steady state response in the phase plane. To analyze this route more accurately, a second order Poincaré map method [37] may be used to evaluate the dynamics of the system.

The evolution of wear for the system is analyzed by following the branches of stable solutions, using an Archard's type wear law to predict wear damage. It has been shown that the beam oscillator can exhibit different work-rates at symmetrically placed contact sites, due to the existence of stable asymmetric orbits [17]. Here it is shown that the differences in work-rate lead to a system which, at least initially, becomes more asymmetric as material is worn off at the contact sites. Two specific cases are analyzed. In the first case, the dynamic response changes and the system becomes more symmetric geometrically as the wear process continues. While, in the second case, the system becomes gradually more asymmetric.

The work-rate, evaluated for stable orbits, is used to predict lifetime of the impacting beam due to fretting wear damage, by extending the branch of stable orbits using the local gap between beam and amplitude constraints as the control parameter. Here lifetime is defined as the time to reach a specified wear depth. The validity of using the work-rate at stable solutions to predict lifetime has been discussed in this paper (Section 6.2.3).

The wear method described here can readily be extended to cover aperiodic response resulting from harmonic as well as stochastic loads, i.e., replacing the fixed point iteration with an averaging method. Furthermore, for industrial applications it will be necessary to consider other processes affecting the gap size, e.g., wear and deformation of the impacting body, wear scar geometry, thermal expansion, friction and environmental effects.

Acknowledgements

The work was supported by the Swedish Foundation for Knowledge and Competence Development (KKS) under Award HÖG 212/01.

Appendix A. Single degree-of-freedom damped harmonic oscillator with elastic constraints

The considered s.d.o.f. oscillator is sketched in Fig. 18. The equation of motion for this system is given as

$$x_{,\tau\tau} + 2\zeta x_{,\tau} + h(x) = \beta\cos(\omega\tau), \tag{A.1}$$

where $h(x) = x$ for $|x|<1$ and $h(x) = w^2x - (w^2-1)\,\mathrm{sgn}(x)$ for $|x|\geqslant 1$. Also, $w^2 = (k_1+k_2)/k_1$, $x = X/X_0$, $\tau = \omega_0 t$, $(\ )_{,\tau} = \partial(\ )/\partial\tau$, $\omega_0^2 = k_1/m$, $2\zeta = c/(m\omega_0)$, $\omega = \Omega/\omega_0$ and $\beta = A/(m\omega_0^2X_0)$. The remaining variables are defined in Fig. 18.

The analytic solution of (A.1) is expressed as

$$x(\tau) = x_{tr}(\tau) + x_{st}(\tau) - \mathrm{sgn}(x_i)(1/w_i^2 - 1), \quad i = \{0,1,\ldots,N\} \tag{A.2}$$

with

$$\begin{aligned}
&x_{tr}(\tau) = \mathrm{e}^{-\zeta(\tau-\tau_i)}\{A_i\cos[\Omega_i(\tau-\tau_i)] + B_i\sin[\Omega_i(\tau-\tau_i)]\},\\
&x_{st}(\tau) = \gamma_i\cos(\omega\tau) + \delta_i\sin(\omega\tau),\\
&A_i = -\gamma_i\cos(\omega\tau) - \delta_i\sin(\omega\tau) + (-1)^i\,\mathrm{sgn}(x_i)/w_i^2,\\
&B_i = [v_i + (-1)^i\,\mathrm{sgn}(x_i)\zeta/w_i^2 + \sin(\omega\tau)(\gamma_i\omega - \delta_i\zeta) - \cos(\omega\tau)(\gamma_i\zeta + \delta_i\omega)]/\Omega_i,\\
&\gamma_i = (w_i^2-\omega^2)\beta/\Delta_i, \quad \delta_i = 2\zeta\omega\beta/\Delta_i,\\
&\Delta_i = (w_i^2-\omega^2)^2 + (2\zeta\omega)^2, \quad \Omega_i^2 = w_i^2 - \zeta^2,
\end{aligned} \tag{A.3}$$

where even and odd i yield motion during contact and free-flight, respectively, e.g., $w_0 = w$ and $w_1 = 1$.

References

[1] F. Pfeiffer, A. Kunert, Ratling models from deterministic to stochastic processes, *Nonlinear Dynamics* 2 (1990) 63–74.

[2] M.J. Pettigrew, C.E. Taylor, N.J. Fisher, M. Yetsir, B.A.W. Smith, Flow-induced vibration: recent findings and open questions, *Nuclear Engineering and Design* 185 (1988) 249–276.

[3] S.W. Shaw, P.J. Holmes, A periodically forced piecewise linear oscillator, *Journal of Sound and Vibration* 90 (1) (1983) 129–155.

[4] S.W. Shaw, The dynamics of a harmonically excited system having rigid amplitude constraints, Part 1: subharmonic motions and local bifurcations, *Journal of Applied Mechanics* 52 (1985) 453–458.

[5] S.W. Shaw, The dynamics of a harmonically excited system having rigid amplitude constraints, Part 2: chaotic motions and global bifurcations, *Journal of Applied Mechanics* 52 (1985) 459–464.

[6] A. Nordmark, Non-periodic motion caused by grazing incidence in an impact oscillator, *Journal of Sound and Vibration* 145 (1991) 279–297.

[7] S. Foale, S. Bishop, Dynamical complexities of forced impacting systems, *Philosophical Transactions of the Royal Society of London* 338 (1992) 547–556.

[8] A. Ivanov, Stabilization of an impact oscillator near grazing incidence owing to resonance, *Journal of Sound and Vibration* 162 (1993) 562–565.

[9] S. Foale, Analytical determination of bifurcations in an impact oscillator, *Proceedings of Royal Society of London A* 347 (1994) 353–363.

[10] C. Budd, F. Dux, Chattering and related behaviour in impacting oscillators, *Philosophical Transactions of the Royal Society of London* 347 (1994) 365–389.
[11] M. Fredriksson, Grazing bifurcations in multibody system, *Nonlinear Analysis Theory: Methods and Applications* 30 (1997) 4475–4483.
[12] D. Wagg, S. Bishop, Chatter, sticking and chaotic impacting in a two-degree of freedom impact oscillator, *International Journal of Bifurcation and Chaos* 11 (2001) 57–71.
[13] M. di Bernardo, C. Budd, A. Champneys, Normalized form maps for grazing bifurcations in *n*-dimensional piecewise-smooth systems, *Physica D* 160 (2001) 222–254.
[14] J. Qiu, Z. Feng, Parameter dependence of the impact dynamics of thin plates, *Computers and Structures* 75 (2000) 491–506.
[15] J. Knudsen, A.R. Massih, Vibro-impact dynamics of a periodically forced beam, *Journal of Pressure Vessel Technology* 122 (2000) 210–221.
[16] J. Knudsen, A.R. Massih, R. Gupta, Analysis of a loosely supported beam under random excitations, in: S. Ziada, T. Staubli (Eds.), *Flow-induced Vibration*, A.A. Balkema, Rotardam, 2000, pp. 505–512.
[17] J. Knudsen, A.R. Massih, Dynamic stability of weakly damped oscillators with elastic impacts and wear, *Journal of Sound and Vibration* 263 (2003) 175–204.
[18] J. Knudsen, Vibro-impact Dynamics of Fretting Wear, Licentiate Thesis, Luleå University of Technology, Luleå, Sweden, 2001.
[19] A.H. Nayfeh, B. Balachandran, *Applied Nonlinear Dynamics*, Wiley, New York, 1995.
[20] T.M. Frick, E. Sobek, J.R. Reavis, Overview on the development and implementation of methodologies to compute vibration and wear of steam generator tubes, in: M. Paidoussis, J. Chenoweth, M. Bernstein (Eds.), ASME Special Publication, *Symposium on Flow-induced Vibrations in Heat Exchangers*, New Orleans, LA, 1984, pp. 149–160.
[21] J. Archard, Contact and rubbing of flat surfaces, *Journal of Applied Physics* 24 (1953) 981–988.
[22] M.J. Pettigrew, M. Yetisir, N.J. Fisher, B.A.W. Smith, C.E. Taylor, Prediction of vibration and fretting-wear damage: an energy approach, in: M.J. Pettigrew (Ed.), *Flow-induced Vibration*—1999, PVP, Vol. 389, ASME, New York, 1999, pp. 283–290.
[23] X. Delaune, E. de Langre, C. Phalippou, A probabilistic approach to the dynamics of wear tests, in: M.J. Pettigrew (Ed.), *Flow-induced Vibration*—1999, PVP, Vol. 389, ASME, New York, 1999, pp. 235–243.
[24] J. Charpentier, T. Payen, Prediction of wear work rate and thickness loss in tube bundles under cross-flow by a probabilistic approach, in: S. Ziada, T. Staubli (Eds.), *Flow-induced Vibration*, A.A. Balkema, Rotardam, 2000, pp. 521–528.
[25] M. Petyt, *Introduction to Finite Element Vibration Analysis*, Cambridge University Press, Cambridge, England, 1990, pp. 386–449 (Chapter 9).
[26] L. Johansson, Beam motion with unilateral contact constraints and wear of contact sites, *Journal of Pressure Vessel Technology* 119 (1997) 105–110.
[27] N. Strömberg, L. Johansson, A. Klarbring, Derivation and analysis of a generalized standard model for contact, friction and wear, *International Journal of Solids and Structures* 33 (1996) 1817–1836.
[28] J. Knudsen, A.R. Massih, L. Johansson, Calculation of vibro-impact dynamics of loosely supported rods, in: *Fluid Structure Interaction, Aeroelasticity, Flow Induced Vibration and Noise*, AD-Vol 53-1, Vol. I, ASME, New York, 1997, pp. 229–237.
[29] J. Knudsen, A.R. Massih, Analysis of a loosely supported beam under harmonic excitation, in: M. Pettigrew (Ed.), *Flow-induced Vibration*—1999, PVP-Vol. 389, ASME, New York, 1999, pp. 265–272.
[30] W.H. Press, S.A. Teukolsky, W.T. Vetterling, B.T. Flannery, M. Metcalf, *Numerical Recipes in Fortran90: The Art of Parallel Scientific Computing*, 2nd Edition, Cambridge University Press, Cambridge, 1996.
[31] J. Rinzel, R.N. Miller, Numerical calculation of stable and unstable periodic solutions to the Hodgkin-Huxley equations, *Mathematical Biosciences* 49 (1980) 27–59.
[32] J.G. Byatt-Smith, 2π periodic solutions of Duffing's equation with negative stiffness, *SIAM Journal of Applied Mathematics* 47 (1) (1987) 60–91.
[33] T.S. Parker, L.O. Chua, *Practical Numerical Algorithms for Chaotic Systems*, Springer, New York, 1989 (Chapter 6).

[34] E. Ott, *Chaos in Dynamical Systems*, Cambridge University Press, Cambridge, UK, 1993.
[35] J. Guckenheimer, P. Holmes, *Nonlinear Oscillations, Dynamic Systems, and Bifurcations of Vector Fields*, Springer, New York, 1986.
[36] E. Grebogi, E. Ott, J. York, Chaotic attractors in crises, *Physical Review Letters* 48 (1982) 1507–1510.
[37] C. Kaas-Petersen, Computation, continuation, and bifurcation of torus solutions for dissipative maps and ordinary differential equations, *Physica D* 25 (1987) 288–306.